Metals and Materials International (2024) 30:1370–1386
https://doi.org/10.1007/s12540-023-01577-6

Analysis of a Full-Scale Bi–Sn Liquid Metal Model for the Continuous Casting of Steel

Hyunjin Yang[1] · Joakim Eck[2] · Pavel Ernesto Ramirez Lopez[2]

Received: 12 August 2023 / Accepted: 6 November 2023 / Published online: 19 December 2023

Abstract

The complex multiphase flow behavior during the continuous casting of steel was investigated through a physically modeled full-scale liquid metal system. This system was operated using a stopper control system (2.5 ton Bi–Sn system). The obtained data, including nozzle pressures, were processed using a concise analytical model. Compared to water modeling, the use of a low-melting-point alloy (58% Bi and 42% Sn eutectic) allows for a full-scale system with material properties closer to those of steel (e.g., interfacial tension). An industrial-scale stainless-steel stopper and a submerged entry nozzle (SEN) were mounted on the system to prevent air permeation due to the negative pressure in the nozzle. Argon gas was injected into an industrial stopper–rod system through an argon line embedded in the stopper. The analytical model characterizes the pressure loss, flow separation, and cavitation of the stopper control system by considering the effects of argon in the nozzle. This study proposes the mapping of the pressure loss, throughput, flow separation, and cavitation based on the gas fraction and stopper position.

Keywords Pressure measurement · Stopper rod control · Flow separation · Pressure loss · Cavitation · Argon

List of Symbols

P	Flow pressure
ρ	Flow density
g	Gravity acceleration
h	Height
V	Flow velocity
P_L	Pressure loss
K	Pressure loss constant
α	Gas volume fraction
d_{gap}	Minimum opening distance at stopper-nozzle gap
P_{argon}	Argon line back pressure
f	Friction factor
Q	Volumetric flow rate
A	Cross section area
h_2	Height difference between tundish bottom and metal level
h_{tun}	Tundish level
h_{tip}	Distance from tundish bottom to stopper tip
L	Length
D	Diameter
h_{sub}	Submergence depth
$h_{stopper}$	Stopper position
P_{nose}	Pressure measured at stopper nose

Subscript

mix	Gas–liquid mixture phase
x_1	Starting point of a streamline
x_2	End point of a streamline
SEN	Submerged entry nozzle
metal	Liquid metal phase
argon	Argon gas phase
gap	Stopper-nozzle gap (opening area)
tun	Tundish
sum	Sum of pressure losses by stopper and argon effects
elbow	Loss by change in the flow direction by port outlet
friction	Friction loss
clog	Loss by clogging
tip	Stopper tip
stopper	Stopper
argon_h	Thermally expanded argon gas
vapor	Vapor pressure of liquid metal

✉ Hyunjin Yang
hyunjin.yang@inha.ac.kr

[1] Department of Mechanical Engineering, Inha University, Incheon 22212, Republic of Korea

[2] Metallurgy Department, Swerim AB, SE 97432 Luleå, Sweden

1 Introduction

Fluid flow is of considerable importance in the continuous casting of steel because it determines the defects and cleanliness of the cast steel. For example, flow instabilities caused by poor flow control lead to recurrent issues such as irregular and deep oscillation marks, interrupted lubrication, and entrapment of slag in the metal bulk and more serious issues such as transverse cracking, mold overflow, and breakouts in the worst-case scenario. Unfortunately, it is challenging to isolate the factors that cause flow instability. These instabilities frequently arise from a combination of factors, including the SEN-stopper design, SEN submergence depth, argon injection, casting speed changes, and product size. Moreover, factors that have no direct relationship with the metal flow play an important role in the emergence of level instabilities. Bulging, clogging, and wearing are clear examples of such cases. These factors combined with inherent turbulent fluctuations in the metal flow produce a complex set of causes for flow-related issues, owing to the high metal feeding rates from the tundish during continuous casting.

Although the influence of flow stability on product quality is a well-known issue, the origin of disturbances, their impact on flow instability, and the corresponding consequences on product quality have mostly been studied separately because of their multidisciplinary nature [1–3]. In particular, disturbances originating from multiphase flows have seldom been studied among the diverse causes [4]. In addition, the behavior of multiphase turbulent flow in a stopper-nozzle-tundish configuration complicates the phenomena owing to several extreme phenomena in the nozzle, along with changes in process variables, including tundish level, casting speed, argon flow rate, immersion depth, and mold size. Thus, there are many related issues that have still not been clearly explained, such as negative pressure occurrence [5–8], air aspiration [9–11], flow separation [12–14], gas accumulation, detachment [10, 15–19] and its relationship to the stopper position, argon flow rate, and throughput. This additional complexity arising near the flow control system, along with the hostile environment of the process (high temperature and pressure conditions), makes studying the multiphase turbulent flow behavior inside the nozzle [20] challenging.

However, several previous studies have attempted to characterize flow patterns and related issues in nozzles using different types of models. The complex behavior of argon gas, associated with flow control systems (e.g., slide gate or stopper rod), has been investigated recently using a lab-scale liquid metal model [19, 21] and a numerical model [4, 10, 22, 23]. The results reveal that the stopper or slide-gate opening is a critical factor that determines not only the throughput of liquid steel but also the amount of pressure loss at the gap, size of the recirculation zones due to flow separation, and bubble size distribution in the mold [10, 19]. In particular, the lab-scale liquid metal model was able to visualize the argon behavior in the nozzle, although it was limited in comparison with the real process because of its simplified geometry and smaller scale. Previous studies have concluded that the stopper position or slide-gate opening should be considered as another factor in understanding the flow pattern in the nozzle, in addition to the ratio between the flow rates of liquid steel and argon gas, which is normally the main factor in flow regime analysis.

Water models have been extended to study multiphase flow issues separately owing to the similarity in kinematic viscosity, optical transparency, and ease of use [7, 11, 24–26]. However, significant differences in wettability and interfacial tension limit the water–air models from reproducing the argon behavior in a real system [27]. In addition, pressure-related phenomena are likely to be underestimated because of the lower density of water. Several previous studies using a water model observed a significant pressure drop near a partially opened nozzle when the stopper position was relatively low (i.e., low throughput). This pressure drop was caused by the continuity effect and pressure loss due to flow separation [8, 22]. The resulting low and negative pressures caused air aspiration in the nozzle and cavitation in extreme cases [7, 8, 11]. These hypotheses were initially deduced from water models and idealized in numerical models.

A 1:1 scale physical model using liquid metal was developed at SWERIM (RFCS project FLOWVIS [28]) to address the shortcomings of the previous physical models. This model uses a low-melting-point Bi–Sn alloy (with physical properties very close to those of steel) to study metal flow through a full-scale submerged entry nozzle (SEN) and mold. As a result, the use of this model facilitates a closer representation of the conditions in a real caster, while simultaneously providing a more permissible environment for developing instrumentation. Extensive operation of the model with diverse measurement techniques revealed initial indications of the importance of stopper regulation and argon injection on flow stability in the mold, along with the identification of critical process issues, such as negative pressure buildup, cavitation, tundish level changes, extreme forces and pressures in the stopper/SEN, stopper-arm rigidity, and nozzle submergence variability.

Bernoulli principle-based models have been widely used to analyze the throughput and pressure in physical models and real casters [7, 8, 29]. A difficulty in applying this approach to a stopper-rod system is the absence of a universal model to quantify the pressure loss occurring in the stopper-nozzle configuration. The pressure loss is strongly dependent on the stopper/nozzle design and

extreme phenomena near the stopper-nozzle gap due to the interrelated casting conditions. Typically, the pressure loss is characterized experimentally by measuring the pressure or throughput, and previous efforts have been made using water model trials [29]. However, to date, the pressure loss by a stopper-rod system has never been characterized with liquid metal in a full-scale system.

There are the differences between the material properties of water and liquid metal. Furthermore, the phenomena occurring in the nozzle and argon line, including flow separation, negative pressure build-up, volumetric expansion during argon injection, gas accumulation, and other multiphase flow effects, are expected to differ. However, there has been no experimental work on this topic using liquid metal, considering the similar configuration and operating conditions as real casting practices at full scale.

Therefore, this study elucidates the relationship between the operating conditions, including the stopper position, argon flow rate, throughput, and corresponding response of the liquid–metal system. The important pressure loss constants for stopper control and argon behavior in the nozzle were characterized by conducting trials using a 1:1 scaled liquid metal model (42% Sn and 58% Bi eutectic alloy). Simultaneously, a 1D analytical model of the throughput of the stopper-rod-based metal delivery system was applied to characterize the measured flow phenomena, such as flow separation and cavitation. An analysis of the pressure data measured from the argon line and stopper tip adjacent to the stopper-nozzle gap quantified the pressure drop and recovery at the gap according to the casting conditions, including stopper position and gas fraction. Consequently, a mapping of the pressure loss and recovery, flow separation, and cavitation for the argon flow rate and stopper position was proposed.

2 Principle of Flow Regulation in Stopper Rod Systems

Continuous casting is a gravity-driven process that uses height difference to deliver superheated liquid steel from a tundish to a mold through an SEN. Because the casting process requires a quasi-steady-state operation (i.e., a stable metal level) for product quality, it is important to balance the incoming liquid steel at the SEN and cast steel exiting the mold. Throughput is determined by the interrelations between the casting conditions, including the casting speed, nozzle design, and stopper position [6, 8]. Industrially, liquid steel throughput is reduced to stabilize the mold level because oversized bore diameters are typically used to cope with clogging events [8]. Therefore, the pouring of liquid steel into a mold is regulated by a flow control system, such as a stopper rod or slide-gate-type valve. During flow regulation, the inlet area of the nozzle was partially closed by a stopper tip, resulting in a narrow concentric annular gap for the flow to pass through (Fig. 1).

A large pressure drop occurs in this open concentric gap because of two mechanisms: flow acceleration and pressure loss [8, 22]. The flow passing through a narrow gap must accelerate to maintain the same flow rate with a smaller cross-sectional area, and the pressure of an accelerated flow decreases according to Bernoulli's principle. In addition, a substantial pressure loss follows owing to the sudden contraction and expansion of the gap; as the accelerated flow cannot adjust to the change in the cross-section owing to its inertia, it may cause flow separation, leading to substantial pressure loss. Therefore, the total pressure drop was significantly affected by the gap area, which was controlled by the stopper position. When the pressure drop was severe, the gauge pressure became negative, resulting in air aspiration through gaps or cracks in the refractory material. Moreover, the negative pressure was transmitted to the argon line, and this negative pressure sucked in air through the porous stopper walls and possible gaps at the line couplings. Oxygen in the infiltrated air reacted with dissolved elements (Al, Si, and Mn), generating non-metallic oxide inclusions such as aluminates and silicates, which are the main sources of nozzle clogging. In extreme cases, the negative pressure at the gap can reach the vapor pressure of the liquid steel. These low pressures may lead to cavitation effects and vaporization of the gases dissolved in the steel. From a flow control perspective, cavitation indicates the limit of the flow control system, as it indicates the inability of the system to further increase throughput.

Other factors include argon injection, clogging, and stopper/nozzle materials [8, 10, 19]. The injected argon may accumulate in the recirculation zones formed by flow

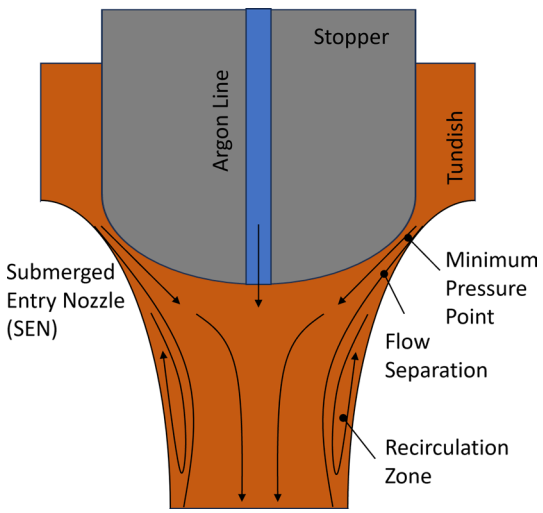

Fig. 1 Configuration of a stopper rod regulation with an SEN

separation and form gas pockets. The interaction between these pockets and the steel flow causes sporadic detachment of large gas bubbles and their subsequent breakup into smaller bubbles owing to the highly turbulent flow. This cycle of pocket buildup, detachment, and breakup causes an irregular flow pattern and unstable throughput. In addition, excessive argon injection with low liquid throughput may shift the flow regime from a bubbly flow to other regimes [20, 30]. All these factors increase the complexity of the issue, making the analysis challenging. However, the regulated gap, controlled by the stopper position, and flow rate of argon injected from the stopper tip are critical factors for the extreme phenomena described above.

3 Analysis of Measurement Data Using Bernoulli Principle

A concise 1D analytical model was applied to characterize the stopper rod regulation. In practice, this model is used to quantify the pressure loss required for a measured throughput in the system and to distinguish the pressure loss into pressure loss due to stopper regulation and argon effects, using the measured argon line pressure.

Figure 2 shows a schematic of the stopper-rod-based metal delivery system used to derive the 1D throughput model. By selecting two arbitrary points (e.g., x_1 and x_2 in Eq. 1) along a streamline connecting the points shown in Fig. 2, the pressure, velocity, and pressure loss of the points, including the associated pressure losses, can be estimated using Bernoulli's equation, as follows:

$$P_{x1} + \rho_{x1} g h_{x1} + \frac{1}{2}\rho_{x1} V_{x1}^2 = P_{x2} + \rho_{x2} g h_{x2} + \frac{1}{2}\rho_{x2} V_{x2}^2 + \sum P_L \tag{1}$$

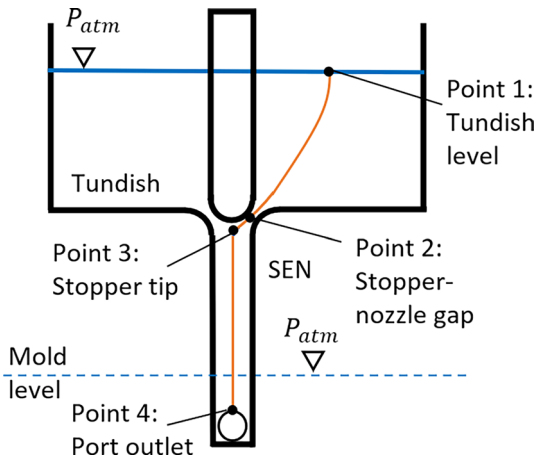

Fig. 2 Paths used for analysis using Bernoulli's principle

Here, the flow properties, including the pressure P, density ρ, and velocity V, were area-averaged over a cross-sectional area, making the model one dimensional (1D).

Most pressure losses ΣP_L can be determined using empirical models. In this model, friction and argon-related losses, as well as pressure losses by the stopper-nozzle gap and port outlet in the SEN are included using the following equation:

$$P_L = K \times \frac{1}{2}\rho_{mix} V_{SEN}^2 \tag{2}$$

Each pressure loss can be calculated by selecting an appropriate pressure loss constant, K. As argon was injected into the SEN after the liquid steel flow passed through the stopper-nozzle gap, the flow velocity in the SEN (V_{SEN}) and the mixture density (ρ_{mix}) was calculated from the measured throughput (Q_{metal}), argon gas flow rate (Q_{argon}), and cross-sectional area (A_{SEN}), assuming a fully developed turbulent flow (i.e., plug flow).

$$V_{SEN} = \frac{Q_{metal} + Q_{argon}}{A_{SEN}} = \frac{Q_{metal}}{A_{SEN}(1-\alpha)} = \frac{Q_{metal}}{A_{eff}}, \tag{3}$$

where α is the average gas volume fraction calculated by,

$$\alpha = \frac{Q_{argon}}{Q_{metal} + Q_{argon}}. \tag{4}$$

The Q_{argon} supplied from the stopper was obtained from the operating conditions, based on the thermal expansion during delivery in the argon line. The ideal gas law considers the increase in gas temperature from room temperature to the operating temperature of a liquid metal system [31]. Similarly, V_{gap} can be calculated using the measured throughput and stopper-nozzle opening area, A_{gap}.

$$V_{gap} = \frac{Q_{metal}}{A_{gap}} \tag{5}$$

Rearranging Bernoulli's equation (Eq. 1) by setting the tundish level and nozzle port outlet (Points 1 and 4 in Fig. 2) as the starting and ending points, respectively, yields the throughput model for the liquid steel:

$$Q_{metal} = A_{SEN}(1-\alpha)\sqrt{\frac{2g\left(\frac{\rho_{metal}}{\rho_{mix}} h_{tun} + h_2\right)}{1 + K_{sum} + K_{elbow} + K_{friction} + K_{clog}}} \tag{6}$$

where K_{sum} is the sum of $K_{stopper}$ and K_{argon}. $K_{stopper}$ is the pressure loss constant for the configuration of the stopper-nozzle gap near the inlet of the SEN, and K_{argon} is the loss constant for the argon-gas-related losses in the nozzle. h_{tun} is the tundish level, and h_2 is the height difference between the tundish bottom and metal level. K_{elbow} is the loss due to the change in the flow direction caused by the port outlet

angle. Pressure loss constants are typically obtained experimentally, because they are empirical factors. In this study, $K_{elbow} = 0.2$ is used based on the SEN design. For friction loss, $K_{friction}$ was obtained using the Darcy–Weisbach equation,

$$K_{friction} = f\frac{L_{SEN}}{D_{SEN}}. \tag{7}$$

where f is the friction factor that depends on Reynolds number and relative roughness, L_{SEN} and D_{SEN} are the length and diameter of SEN respectively. Physically, $K_{friction}$ quantifies the pressure loss by wall friction resistance when the liquid metal flows in the SEN. The pressure loss due to clogging can be accounted for by selecting a suitable K (i.e., K_{clog}) in Eq. 2, if needed. K_{clog} was set to zero for the analysis because clogging was not observed during the trial. In this study, $K_{stopper}$ and K_{argon} were characterized using the data obtained from full-scale liquid metal trials.

Because the throughput of the system is controlled in the full-scale liquid metal model using the pump speed (RPM), the throughput model (Eq. 6) can be used to estimate the total pressure loss K_{sum}, including $K_{stopper}$ and K_{argon} in the system. Because other pressure loss constants ($K_{elbow}$and $K_{friction}$) can be obtained using the empirical equations above, the throughput model provides the sum of the unknown pressure losses (i.e., $K_{sum} = K_{stopper} + K_{argon}$) due to stopper regulation and argon effects in the nozzle.

Similarly, the approach using Bernoulli's equation can be applied for a different endpoint (the stopper tip instead of the nozzle port outlet, i.e., Points 1 and 3 in Fig. 2), to directly calculate $K_{stopper}$ based on the measured argon line pressure. With the pressure at the stopper tip (P_{tip}) indirectly measured through the argon line, $K_{stopper}$ is characterized by rearranging Eq. 1 as follows:

$$K_{stopper} = \frac{\rho_{metal} g\left(h_{tun} + h_{tip}\right) - P_{tip} - \frac{1}{2}\rho_{mix} V_{SEN}^2}{\frac{1}{2}\rho_{mix} V_{SEN}^2} \tag{8}$$

where h_{tip} is the distance from the tundish bottom to stopper tip. Once $K_{stopper}$ was obtained, K_{argon} was estimated by subtracting $K_{stopper}$ from K_{sum} calculated from the throughput model ($K_{sum} = K_{stopper} + K_{argon}$). Here, K_{argon} includes all argon-related effects in the nozzle below the stopper-nozzle gap. The measurement data is processed from a macroscopic perspective so that how much pressure loss would be expected in the entire nozzle when an operator injects a certain amount of argon gas. With K_{sum}, $K_{stopper}$, and K_{argon} characterized using the 1D throughput model, flow separation can be identified using the simple criterion, $K_{stopper} > K_{sum}$. As $K_{stopper}$ is supposed to be a portion of K_{sum} according to its definition ($K_{sum} = K_{stopper} + K_{argon}$), $K_{stopper}$ must not exceed K_{sum}, calculated based on the measured pump speed (RPM). The flow velocity at the stopper tip V_{tip} was updated using the following equation if the criterion $K_{stopper} > K_{sum}$ is satisfied:

$$V_{tip} = V_{SEN}\sqrt{1 + K_{stopper} - K_{sum}} \tag{9}$$

The updated V_{tip} allowed the same pressure to be obtained as the pressure at the stopper tip P_{tip}, which was monitored during the trials through the argon line. The pressure loss constant for stopper $K_{stopper}$ was corrected to be the same as the sum K_{sum} (i.e., $K_{stopper} = K_{sum}$), and K_{argon} was treated as zero. The flow velocity V_{tip} remained the same as the velocity in the nozzle V_{SEN}, if flow separation did not occur, because the plug flow assumption is valid in such cases. Figure 3 summarizes the process in a flow chart below:

Using the throughput Q_{metal} obtained in Eq. 6, the pressure at the stopper-nozzle gap P_{gap}, where the minimum gap opening exists, can also be expressed mathematically. This is achieved by rearranging Bernoulli's equation (Eq. 1) with a path from the tundish level to the gap (Points 1 and 2 in Fig. 2).

$$P_{gap} = \rho_{metal} g h_{tun} - \frac{1}{2}\rho_{metal}\left(\frac{Q_{metal}}{A_{gap}}\right)^2 \tag{10}$$

Therefore, applying Bernoulli's principle enables the characterization of pressure loss constants for stopper

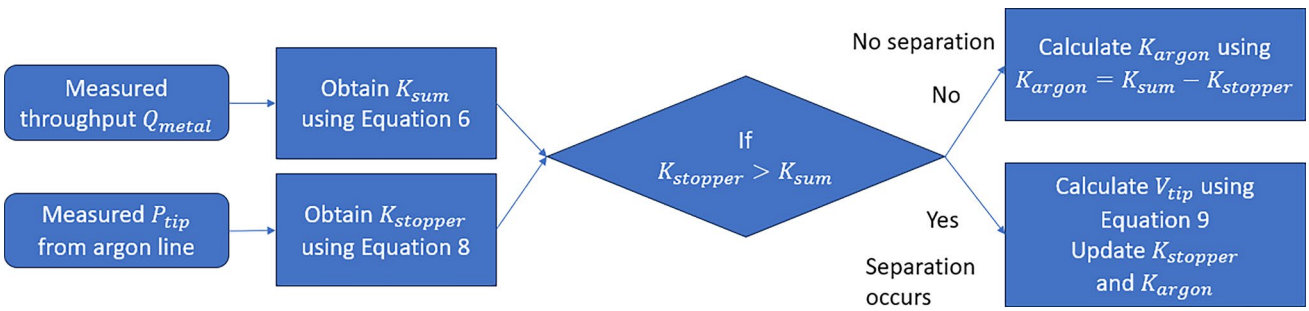

Fig. 3 Flow chart for characterizing pressure loss constants and flow separation

regulation and argon-related effects, along with flow separation and minimum gap pressure. This simple but systematic methodology was implemented for experimental data collected from a full-scale liquid metal model.

4 Experiment Setup: CCS Geometry and Operating Conditions

A full-scale continuous casting simulator (CCS) at Swerim AB (Luleå, Sweden) was used to measure the flow properties of the liquid metal during the casting trials. The study of complex flow phenomena in industrial casters presents several challenges, including instrumentation and safety issues. Thus, the current work uses a liquid metal model based on a Bismuth–Tin alloy (Bi 52%, Sn 48%, melting point = 137 °C), which has very similar properties as liquid steel at much lower temperatures (150–200 °C). At a scale of 1:1, this model can realistically simulate the behavior of liquid steel in a caster, including the effects of flow regulation at the metal level (Fig. 4). The lower operational temperatures of the CCS (160 ℃) facilitate the development and implementation of monitoring tools, which can provide a more complete picture of the phenomena occurring during flow regulation. Table 1 summarizes the CCS specifications and material properties of the eutectic Bi–Sn alloys.

The CCS operates as industrial slab casters by delivering liquid metal from a tundish to a mold through a SEN. A stopper regulates the throughput of the gravity-driven flow by controlling the inlet area of the SEN. As shown in Table 1, the scale of the model is within the range of common industrial slab casters. The difference between the CCS and a real caster is that the CCS is a closed-loop system; instead of the solidified shell being pulled into the secondary cooling, the metal is circulated to the tundish through a centrifugal pump without solidification. The heating elements were located at the bottom of the mold to prevent the solidification of the metal. The bottom was inclined to allow the liquid metal to pass through a pump tank located next to the mold.

The centrifugal pump submerged in the pump tank determined the flow rate of the liquid metal delivered to the tundish based on its rotational speed (RPM). Four heating elements were placed in the vessel of the pump to ensure that the alloy was molten. Among these, two were at the bottom, consistently in the mold, while an additional two short elements were positioned further up in the vessel.

The tundish level was maintained at a certain level, by continually supplying liquid metal to the tundish. The level was set according to the mass balance between the incoming

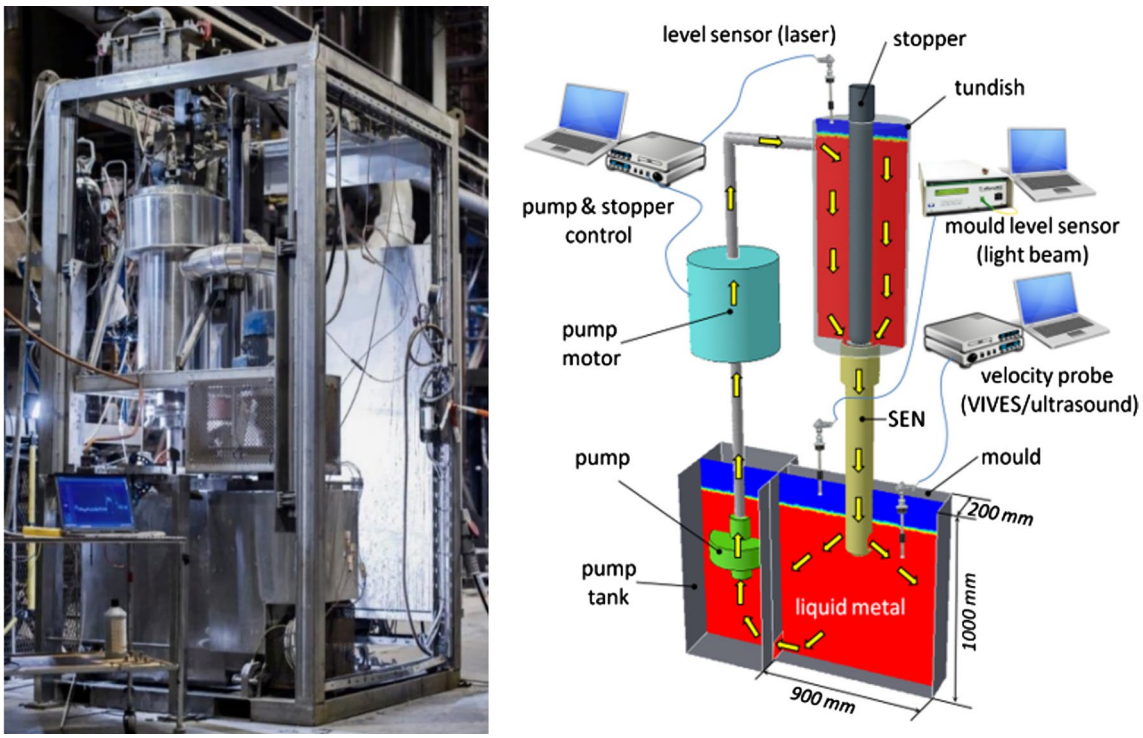

Fig. 4 Full-scale continuous casting simulator (CCS)

Table 1 CCS specifications and material properties of Bi–Sn alloy

Mold size	Width: 1200 mm, thickness: 220 mm, height: 920 mm
Total mass of liquid metal	3.375 tons
Casting speed	0–1.022 m/min
Throughput	0.0045 m^3/s (2.265 tons/min)
Argon flow rate	Up to 7 SLPM
Stopper position	0 mm (fully closed) to 7 mm (fully open)
Tundish level	800–900 mm
Tundish volume	0.044 m^3 (D = 0.25 m, H = 0.9 m, cylindrical shape)
Immersion depth	Up to 700 mm
SEN bore diameter	73 mm
SEN length	965 mm
Port outlet	68 mm (height) by 56.3 mm (width)
Port angle, length	5 degrees downward, 23 mm
Stopper length	910 mm
Stopper diameter	114 mm
Argon line axial bore diameter	9.728 mm

	Viscosity (Pa.s)	Density (kg/m^3)	Surface tension (N/m)	Electrical conductivity $(\Omega m)^{-1}$
Steel (1600 °C)	0.0063	7000	1.0–1.8	0.7×10^6
Bi–Sn alloy MCP 137 (160 °C)	0.00965	8580	0.430	1.0×10^6
Water (25 °C)	0.001	998	0.0728	Not applicable

flow from the pump and outgoing flow through the SEN. The flow inlet was located in the middle of the tundish to minimize contact with air. To ensure safety, the tundish was surrounded by another vessel connected to a pump tank.

The stopper position was controlled by an operator to maintain a stable tundish level, which was monitored during the trial using a level sensor. The stopper position was adjusted using a hydraulic system via a processing computer. The argon flow rate from a gas supply tank under standard conditions was controlled using a flow meter, and the consequent back pressure in the argon line was measured like industrial casters. The back pressure of the argon line was continuously measured during the trial using a piezoresistive pressure sensor, which estimated the flow pressure from the deformation of a piezoresistive element attached to a diaphragm. Another pressure sensor was embedded in the surface of the stopper nose to directly measure the flow pressure in the nozzle. It was located 3 cm from the stopper tip (where the argon line outlet was located), to measure the static pressure of the flow near the nozzle-stopper gap. A fiber-optic pressure sensor was deployed to measure low pressures due to the narrow cross-sectional area of the nozzle. A stainless stopper and SEN were used for the trial to ensure effective sealing in the flow delivery system. This facilitated the achievement of a negative pressure near absolute zero in the nozzle, thereby inducing cavitation.

The submergence depth of the nozzle (distance from the metal level to the top of the port outlet) is another operating condition that can be adjusted during the trial in two ways. The relative position between the tundish and mold can be modified by elevating the tundish through a hydraulic system. However, the metal level in the mold can vary like a real process based on the mass balance between the incoming and outgoing flows. In the CCS, the outgoing flow is due to the pump rather than the solidified shell, which is controlled by the casting speed. Thus, the rotational speed of the pump was determined based on the casting speed in the simulated practice. Silicon oil was applied at the metal level to prevent oxidation of the liquid metal during the trial.

Therefore, five casting parameters were adjusted during the trial using CCS like industrial casters: (1) casting speed (i.e., pump rotational speed), (2) argon flow rate, (3) stopper position, (4) tundish level, and (5) submergence depth. The operating ranges of the casting parameters are listed in Table 1. All the casting conditions were recorded at a sampling frequency of 2 Hz. Under the casting conditions, the pressure measurements from the argon line and stopper nose adjacent to the nozzle-stopper gap were measured transiently with an 8 Hz sampling frequency.

5 Measurement Data and Characterized Properties

Table 2 shows casting conditions and corresponding pressure measurements during the CCS trials. 35 process points covering a casting speed from 0.43 to 1.0 m/min (0.967 to 2.286 tons/min throughput) with an argon flow rate Q_{argon} from 0 to 4 SLPM are obtained from the corresponding quasi-steady state during the operation. The submergence depth of SEN (h_{sub}) was maintained at 300 mm, with the tundish level (h_{tun}) between 800 and 900 mm. Measured argon flow rate Q_{argon} at the inlet of argon line under standard condition was converted into the actual gas flow rate into the nozzle at the stopper tip Q_{argon_h}, as discussed in Sect. 3. Thus, the gas fraction α in Table 2 includes thermal expansion of argon flow due to the operating temperature of CCS (160 °C). On the other hand, the pressure effect is not included in this work because the change of gas pressure during delivery was marginal (pressure drop ≅ 100 Pa): the argon line has a constant diameter without any special treatment. This leads to the conclusion that the back pressure (P_{argon}) measured from the inlet of argon line represents the pressure at the stopper tip (outlet of argon line). It is a useful finding as the indirect pressure measurement through the argon line is very close to the flow pressure in the SEN. Therefore, the thermal expansion effect is the main factor of gas volume change during gas delivery to the system. The argon bubbles injected from the stopper tip is expected to flow into the SEN by following the metal flow because the drag force applied on the bubble (around $d = 5$ mm according to the argon line diameter) is greater than the buoyancy force. The measured stopper position $h_{stopper}$ was converted into a corresponding opening area of the nozzle using the curve in Fig. 5. A computer-aided-design (CAD) geometry is used to measure the minimum distance d_{gap} and minimum opening gap area A_{gap} between the stopper nose and nozzle, for a given stopper position. Figure 5 shows an interpolated polynomial function based on the measured opening areas. This function varies with the stopper nose and SEN inlet shape.

Two pressure measurements from the back pressure of the argon line P_{argon} and stopper nose P_{nose} adjacent to the minimum gap (30 mm from the stopper tip, as shown in Fig. 6b) are shown under the given casting conditions. The raw data collected from the pressure sensors were smoothed using moving averages for 50 s. In addition to the measurement data, the flow pressure at the minimum gap area P_{gap} was estimated under the given casting conditions using Eq. 10. Thus, the three pressure points (P_{argon}, P_{nose}, and P_{gap}) describe how the flow pressure evolves in the stopper-nozzle gap. The difference between the pressures measured at the argon line and nose is defined as the pressure recovery, $P_{recovery}$ ($P_{recovery} = P_{argon} - P_{nose}$), and the values are listed in Table 2.

In addition, the characterized pressure loss constants for the stopper regulation $K_{stopper}$, argon effects K_{argon}, sum of the two losses K_{sum}, and flow velocity at the stopper tip V_{tip}, at the nozzle-stopper gap V_{gap}, and in the nozzle V_{SEN} are listed in Table 2. V_{gap} and V_{SEN} were calculated using Eqs. 5 and 3, respectively, using the measured throughput Q_{metal} and geometry given in Table 1 and Fig. 5, respectively. The flow separation was identified using the criterion shown in Fig. 3. A flow separation event occurs if the estimated flow velocity at the tip V_{tip} (Eq. 9) differs from the flow velocity in the nozzle V_{SEN} (i.e., $V_{tip} \neq V_{SEN}$). The severity of flow separation was quantified as a separation index, by rating it between 0 and 1 using the following equation:

$$Sep = \frac{V_{tip} - V_{SEN}}{V_{gap} - V_{SEN}} \tag{11}$$

Similarly, a cavitation event is identified when the estimated pressure at the gap (P_{gap} in Eq. 10) is lower than the vapor pressure of the liquid metal ($P_{gap} < P_{vapor}$). In practice, the gap pressure P_{gap} is unlikely to be lower than the vapor pressure of the liquid metal because the gas formed by cavitation maintains the flow pressure. However, the calculated gap pressure P_{gap} is still a useful indicator of cavitation.

Figure 7 shows the measured pressures mapped in 3D with a specific stopper position and argon flow rate; the measured pressure from the argon line (Fig. 7a) was compared with the pressure measured at the stopper nose (Fig. 7b). It is found that pressures directly measured from the stopper nose are lower than those from the argon line. This indicates that the actual flow pressure in the nozzle is lower than the indirectly measured pressure by the argon line back pressure, which is typically used for monitoring industrial casters. Note that direct pressure measurement during industrial practices is challenging due to the harsh operating conditions. Thus, it is suggested that the pressure from the argon line should be interpreted with caution as the actual flow pressure is likely to be lower than the monitored readings. The 3D surfaces interpolated based on the pressures of each measurement point showed similar trends with regard to the stopper position and argon flow rate, with both showing positive correlations with the argon flow rate and negative correlations with the stopper position. Namely, the flow pressure decreases as the stopper is lifted while the pressure increases as the argon flow rate increases in both measurements.

Table 2 Casting conditions with measurement data for process points during trials (C: Calculated, M: Measured)

Period	Pump rpm	Q_metal	Casting speed	Q_argon	Q_argon_h	Gas fraction	h_stopper	d_gap	h_tun	h_sub	P_argon	P_nose	P_recovery	P_gap	Cavitation	K_sum	K_stopper	K_argon	K_friction	V_gap	V_tip	V_sen	Separation #	Seperation
	[RPM]	[m3/s]	[m/min]	[SLPM]	[LPM]	NA	[mm]	[mm]	[mm]	[mm]	gauge [Pa]	gauge [Pa]	gauge [Pa]	gauge [Pa]	Y/N	NA	NA	NA	NA	[m/s]	[m/s]	[m/s]	NA	Y/N
Measured Calculated	M	M	M	M	C	C	M	M	M	M	M	M	M	C	C	C	C	C	C	C	C	C	C	C
1	900	0.001879	0.427119893	2	2.9501	0.0174278	2.207	1.15552	860	300	-5706	-101600	95894	-56237	N	150.81	89.901145	60.9052	0.6433	5.47495	0.4608	0.4608	0	N
14	1029	0.002628	0.597177549	4	5.8366	0.0247441	2.92	1.6038	886	300	10490	-19610	30100	-46841	N	76.305	37.02583	39.2789	0.6369	5.31929	0.651	0.651	0	N
15	1029	0.002628	0.597177549	1	1.4777	0.006303	3.032	1.67304	837	300	-7032	-34220	27188	-61567	N	77.032	45.932919	31.0995	0.6369	5.54676	0.6337	0.6337	0	N
16	1040	0.002688	0.610842137	2	2.9501	0.0122502	3	1.65327	899	300	2533	-33810	36343	-54397	N	75.467	41.044095	34.4226	0.6365	5.50555	0.6539	0.6539	0	N
17	1040	0.002688	0.610842137	4	5.8366	0.024204	3.096	1.7126	885	300	9909	-27040	36949	-46784	N	72.889	35.644341	37.2448	0.6365	5.31619	0.6654	0.6654	0	N
2	1051	0.002747	0.624382584	2	2.9501	0.0119878	2.798	1.52823	866	300	-18040	-98770	80730	-56587	N	70.717	48.730491	21.9864	0.6362	5.49313	0.6681	0.6681	0	N
39	1051	0.002747	0.624382584	0	0	0	3.066	1.69406	874	300	NA	NA	NA	-85188	N	72.996	72.995958	0	0.6362	6.08261	2.5535	0.6564	0.34961243	Y
40	1051	0.002747	0.624382584	2	2.9501	0.0119878	3.208	1.78186	848	300	NA	NA	NA	-45713	N	69.912	38.507558	31.4045	0.6362	5.22366	0.6681	0.6681	0	N
25	1070	0.002849	0.647482902	0	0	0	2.8	1.52947	836	300	-81820	-101987	20167	-100074	N	66.144	66.143714	0	0.6356	6.3026	2.2834	0.6807	0.28507667	Y
29	1070	0.002849	0.647482902	2	2.9501	0.011565	3.314	1.84754	854	300	-3452	-22539	19087	-45244	N	65.196	37.560641	27.635	0.6356	5.22445	0.6924	0.6924	0	N
26	1081	0.002907	0.660692894	0	0	0	2.838	1.55303	883	300	-82361	-100589	18228	-97870	N	65.363	65.363495	0	0.6353	6.3349	2.3184	0.6946	0.28788762	Y
27	1081	0.002907	0.660692894	3	4.4052	0.0169088	3.405	1.9041	870	300	2985.92	-18872	21857.92	-78342	N	62.44	33.348655	29.0917	0.6353	5.94341	0.7121	0.7121	0	N
3	1132	0.00317	0.72042017	2	2.9501	0.0104063	3.156	1.74969	870	300	-24150	-97060	72910	-62546	N	52.987	39.022771	13.9644	0.634	5.62511	0.7691	0.7691	0	N
37	1132	0.00317	0.72042017	2	2.9501	0.0104063	3.413	1.90908	890	300	-8295	-26011	17716	-44568	N	53.661	33.351596	20.309	0.634	5.27668	0.7691	0.7691	0	N
38	1132	0.00317	0.72042017	0	0	0	3.613	2.0342	882	300	-88051	-77074	-10977	-87396	N	54.65	54.650068	0	0.634	6.13758	2.6206	0.7574	0.34631799	Y
4	1233	0.00366	0.831828386	2	2.9501	0.0090252	3.561	2.00155	870	300	-20050	-94410	74360	-73268	N	39.412	27.84846	11.563	0.6321	5.84305	0.8862	0.8862	0	N
30	1233	0.00366	0.831828386	0	0	0	3.749	2.12004	873	300	-93971	-86621	-7350	-91087	N	40.304	40.304327	0	0.6321	6.19303	2.932	0.8745	0.38686001	Y
31	1233	0.00366	0.831828386	2	2.9501	0.0090252	3.769	2.13272	874	300	-36500	-16193	-20307	-71170	N	39.513	32.897285	6.61544	0.6321	5.80781	0.8862	0.8862	0	N
5	1341	0.004145	0.942022026	2	2.9501	0.0079779	3.959	2.25398	878	300	-37660	-70980	33320	-90063	N	30.56	25.823366	4.73632	0.6307	6.18166	1.0021	1.0021	0	N
32	1341	0.004145	0.942022026	2	2.9501	0.0079779	3.979	2.26683	870	300	-73558	-64634	-8924	-92646	N	30.402	30.401584	0	0.6307	6.21757	2.1714	1.0021	0.22420058	Y
33	1341	0.004145	0.942022026	0	0	0	3.997	2.27841	891	300	-92060	-74532	-17528	-87275	N	31.384	31.384425	0	0.6307	6.14965	2.9233	0.9903	0.37465436	Y
6	1411	0.004441	1.009205721	2	2.9501	0.0074507	3.961	2.25527	810	300	-67730	-91370	23640	-109236	Y	25.252	25.25195	0	0.6299	6.43028	1.896	1.0727	0.15366977	Y
7	1411	0.004441	1.009205721	1	1.4777	0.0037393	3.965	2.25783	843	300	-79810	-98590	18780	-109815	Y	26.045	26.045122	0	0.6299	6.49083	2.5124	1.0668	0.26650799	Y
8	1411	0.004441	1.009205721	0.5	0.7391	0.0018732	3.965	2.25783	865	300	-85930	-84980	-950	-111724	Y	26.541	26.541224	0	0.6299	6.558	2.7708	1.0639	0.31068713	Y
9	1411	0.004441	1.009205721	0	0	0	4.007	2.28484	857	300	-93960	-97960	4000	-113034	Y	26.518	26.517664	0	0.6299	6.56931	3.0419	1.061	0.35961787	Y
10	1411	0.004441	1.009205721	1	1.4777	0.0037393	4.013	2.28871	857	300	-82740	-92590	9850	-117577	Y	26.288	26.287702	0	0.6299	6.64942	2.6455	1.0668	0.28278765	Y
11	1411	0.004441	1.009205721	2	2.9501	0.0074507	4.041	2.30676	860	300	-78470	-92170	13700	-117325	Y	26.114	26.113569	0	0.6299	6.64942	2.4751	1.0727	0.25146722	Y
12	1411	0.004441	1.009205721	3	4.4052	0.0111346	4.047	2.31063	865	300	-50490	-83120	32630	-117345	Y	25.979	24.655081	1.32391	0.6299	6.65713	1.0785	1.0785	0	N
13	1411	0.004441	1.009205721	4	5.8366	0.0147913	4.049	2.31193	883	300	-18240	-56560	38320	-75680	N	26.072	18.293691	7.77808	0.6299	5.91256	1.0842	1.0842	0	N
19	1411	0.004441	1.009205721	4	5.8366	0.0147913	4.082	2.33325	839	300	-18340	-59650	41310	-79701	N	25.322	17.563768	7.75782	0.6299	5.91884	1.0842	1.0842	0	N
20	1411	0.004441	1.009205721	2	2.9501	0.0074507	4.084	2.33455	848	300	-74670	-97150	22480	-109601	Y	25.907	25.906781	0	0.6299	6.49453	2.287	1.0727	0.22396535	Y
21	1411	0.004441	1.009205721	0	0	0	4.152	2.37863	850	300	-87970	-100100	12130	-110053	Y	26.396	26.395702	0	0.6299	6.50565	2.803	1.061	0.31994643	Y
22	1411	0.004441	1.009205721	2	2.9501	0.0074507	4.156	2.38123	846	300	-71020	-97260	26240	-106006	Y	25.872	25.872316	0	0.6299	6.42665	2.0905	1.0727	0.19010198	Y
35	1411	0.004441	1.009205721	0	0	0	4.384	2.53028	876	300	-94592	-83583	-11009	-96459	N	26.849	26.848705	0	0.6299	6.50565	3.066	1.061	0.36825213	Y
36	1411	0.004441	1.009205721	2	2.9501	0.0074507	4.388	2.53291	867	300	-69084	-72202	3118	-97596	N	26.234	26.234196	0	0.6299	6.30503	1.9784	1.0727	0.17308962	Y

5.1 Characterization of Pressure Loss (K_{sum}, $K_{stopper}$, and K_{argon})

Figure 8 shows the behavior of the pressure loss K_{sum}, which includes the pressure loss by stopper control and argon-related effects. K_{sum} is plotted with respect to the stopper position in Fig. 8. A regression line was obtained for each Ar flow rate based on the data corresponding to each process point in Table 2. As expected, the pressure loss K_{sum} showed a strong negative correlation with the stopper position, such that the pressure loss K_{sum} decreased as the stopper was lifted. The slope of the regression line became steeper as the argon flow rate increased to 3 SLPM and then decreased at 4 SLPM: It appears that the slope of the regression line for K_{sum} has decreased in 4SLPM due to the increase of K_{sum} at a high stopper position (e.g., $h_{stopper}$ = 4.4 mm). The magnitude of the pressure loss, K_{sum} seems to increase with the argon flow rate, but the difference decreased as the stopper position approached 4 mm.

The pressure loss was further characterized by decomposing K_{sum} into $K_{stopper}$ and K_{argon} according to the criterion discussed in Fig. 3: The two pressure losses plotted in Fig. 9 show opposite behavior for argon injection: the pressure loss by stopper $K_{stopper}$ decreases with the argon flow rate, whereas the pressure loss by argon K_{argon} increases with it. Because $K_{sum} = K_{stopper} + K_{argon}$, the proportion of $K_{stopper}$ in K_{sum} decreases as the argon flow rate increases by the increase of K_{argon}. With 4 SLPM of argon injection, the K_{argon} and $K_{stopper}$ portions became similar: Since the contribution of the argon effect in the K_{sum} increases with a higher argon flow rate, the sum of argon and stopper effects, K_{sum}, goes up with K_{argon} and it makes the slope of the regression line for 4SLPM in Fig. 8 decrease. The pressure loss by argon effects K_{argon} approached zero as the stopper position increased. This indicates that the loss due to the effects of argon diminishes as the gas fraction α decreases with an increase in the liquid metal throughput Q_{steel}.

Figure 10a shows a comparison of the predicted throughput with the measured data. The regression equations obtained for K_{sum} in Fig. 8b were used for predicting the throughput (Eq. 6, $K_{sum} = K_{stopper} + K_{argon}$). The calculated throughput represents the displayed measurement points. The stopper gain for the argon flow rate was obtained by taking the slopes of the throughput curves in Fig. 10a. Physically, the stopper gain provided the expected increase in throughput by lifting the stopper. The stopper gain appeared to increase with the argon flow rate of up to 3 SLPM, implying that the throughput Q_{metal} became more sensitive to the stopper position as more argon was injected.

5.2 Characterization of the Flow Separation

The separation index introduced in Eq. 11 was applied to identify the flow separation in the nozzle. Figure 11 compares the separation index for argon injections of 0 SLPM (Fig. 11a) and 2 SLPM (Fig. 11b). The separation index indicates the severity of flow separation by normalizing the flow velocity in the nozzle between 0 and 1. The flow separation occurs at all process points without argon injection, indicating that the index is always greater than zero. The separation index for 2 SLPM is zero up to a stopper position of 4 mm, corresponding to around 2.2 tons/min of throughput. This implies that flow separation can be avoided with 2 SLPM of argon injection, unlike for the same throughput without argon injection. As shown in Table 2, flow separation was not observed with 4 SLPM of argon injection in the operation range tested in this study. This confirmed that the argon injection was effective in suppressing the flow separation. This result aligns with the observation of a higher $K_{stopper}$ for scenarios without argon injection in comparison to the cases with 2 SLPM, as shown in Fig. 9a, because flow separation leads to an increase in pressure loss.

5.3 Characterization of Pressure Recovery

Figure 12 shows the flow pressure variation near the stopper opening, by quantifying the measured pressure difference ($P_{recovery} = P_{argon} - P_{nose}$). A positive pressure recovery ($P_{recovery} > 0$) can be expected owing to the continuity effect. The continuity effect occurs because the cross-sectional area widens as the flow exits from the stopper-nozzle gap to the nozzle. Pressure recovery is beneficial for continuous casting because it narrows the negative pressure region in the nozzle. However, the continuity effect may not be achieved if flow separation occurs in the nozzle. In such cases, $P_{recovery}$ may be low or negative because flow separation generates further pressure loss by viscous dissipation in the recirculation zones (Fig. 1). Figure 12 reveals that argon injection helps pressure recovery; $P_{recovery}$ is positive at most of the process points with argon injection, while the recovery becomes less than 20,000 Pa without argon injection. In some severe cases, a negative pressure recovery (i.e., $P_{recovery} < 0$) was observed in the absence of argon. This implies that further pressure loss by flow separation lowers the flow pressure even after passing through the narrow stopper-nozzle gap.

5.4 Characterization of Cavitation

Figure 13 shows the relationship between the throughput of the liquid metal (Q_{metal}) and pressure at the minimum gap (P_{gap}). The points represent the measurement data from each process point, whereas the solid lines are

the gap pressures (P_{gap}) predicted via Eq. 10, using the throughput of the system Q_{metal} (Eq. 6), pressure loss K_{sum} ($K_{sum} = K_{stopper} + K_{argon}$) obtained in Fig. 8, and A_{gap} given in Fig. 5a. As expected from the mathematical form of Eq. 10, P_{gap} appears as a concave function for Q_{metal}.

Starting from the peak of the curve, where the flow velocity at the gap V_{gap} ($V_{gap} = \frac{Q_{metal}}{A_{gap}}$) becomes minimum, P_{gap} decreases with both the increase and decrease in the throughput because of the increase in V_{gap}. For instance, V_{gap} increases even though the throughput Q_{steel} reduces from the peak point of the curve, since the rate of decrease of A_{gap} is greater than Q_{metal} (i.e., gap size dominant). Similarly, the opposite situation also leads to an increase in V_{gap} because the rate of increase of Q_{metal} is greater than A_{gap} (i.e., throughput-dominant), when the throughput increases from the peak point. The varying rate of A_{gap} was determined using the nozzle and stopper designs used in the trials. The peak of the curve appears to increase with the argon flow rate, which aligns with typical industrial casting practices, in which the negative nozzle pressure is alleviated by argon injection.

Figure 13 shows that the throughput range of the system is constrained by two factors: 1) the operating range of the stopper and 2) vapor pressure of the working fluid. With the curves drawn within the operating range of the liquid metal system ($h_{stopper}$ = 0–7 mm), the lower limit of the predicted gap pressure P_{gap} was determined using the vapor pressure of the liquid metal, which is displayed as a broken horizontal line in Fig. 13. Thus, the throughput Q_{metal} cannot be increased or decreased further once the system reaches a cavitation state at the stopper-nozzle gap (i.e., $P_{gap} < P_{vapor}$), even though the operating range of the stopper can change the gap opening. The obtained throughput window, constrained by cavitation and the operating range of the stopper, appeared to widen with argon injection, by shifting of the entire curve upward (Fig. 13). This shift was accompanied by an increase in the gap pressure P_{gap}, which is favorable for industrial casting practices.

5.5 Correlation Analysis of Key Properties

Table 3 gives the Pearson correlation coefficients obtained from a correlation analysis between the selected process parameters (stopper position $h_{stopper}$ and gas fraction α) and pressure-related outputs shown in Table 2. As shown in Figs. 9 and 10, all the pressure loss coefficients characterized in this study showed a negative correlation with the stopper position. This led to lower flow pressures such as P_{argon} and P_{gap}. The gas fraction showed a strong positive correlation with the argon line pressure P_{argon} and pressure loss coefficient for the argon effects K_{argon}. In addition, the strong negative correlation between the gas fraction and separation index indicates that argon injection is an effective measure to suppress the flow separation, which expedites positive pressure recovery through the continuity effect and provides a higher flow pressure at the tip of the stopper P_{argon}.

6 Conclusions

1. The actual flow pressure at the stopper-nozzle gap was likely to be lower than that measured from the argon line of the nozzle. Therefore, caution should be exercised when interpreting the negative pressure readings observed using the argon line, during industrial casting practices.
2. A correlation analysis of the measurement data confirmed that the nozzle pressures exhibited negative and positive correlations with the stopper position and argon flow rate, respectively.
3. The pressure loss constant for stopper regulation ($K_{stopper}$) and argon-related effect (K_{argon}) and sum of the two loss constants (K_{sum}) were all characterized as linear functions. Moreover, the portion of K_{argon} contributing to K_{sum} became more significant with increasing argon flow rates.
4. Argon injection is effective in suppressing the flow separation and promoting pressure recovery at the stopper-nozzle gap. The throughput achievable while avoiding flow separation depends on the argon flow rate.
5. The characterized pressure loss enabled the estimation of the throughput range, based on the cavitation at the stopper-nozzle gap. Argon injection helped widen the throughput range by increasing the pressure at the gap where cavitation was likely to occur.

The characterization methodology introduced in this study is useful for assessing the performance of the stopper control systems, widely used in the steel industry. An appropriate throughput range while maintaining a positive nozzle pressure can be achieved by optimizing the operating window and improving the stopper and nozzle designs.

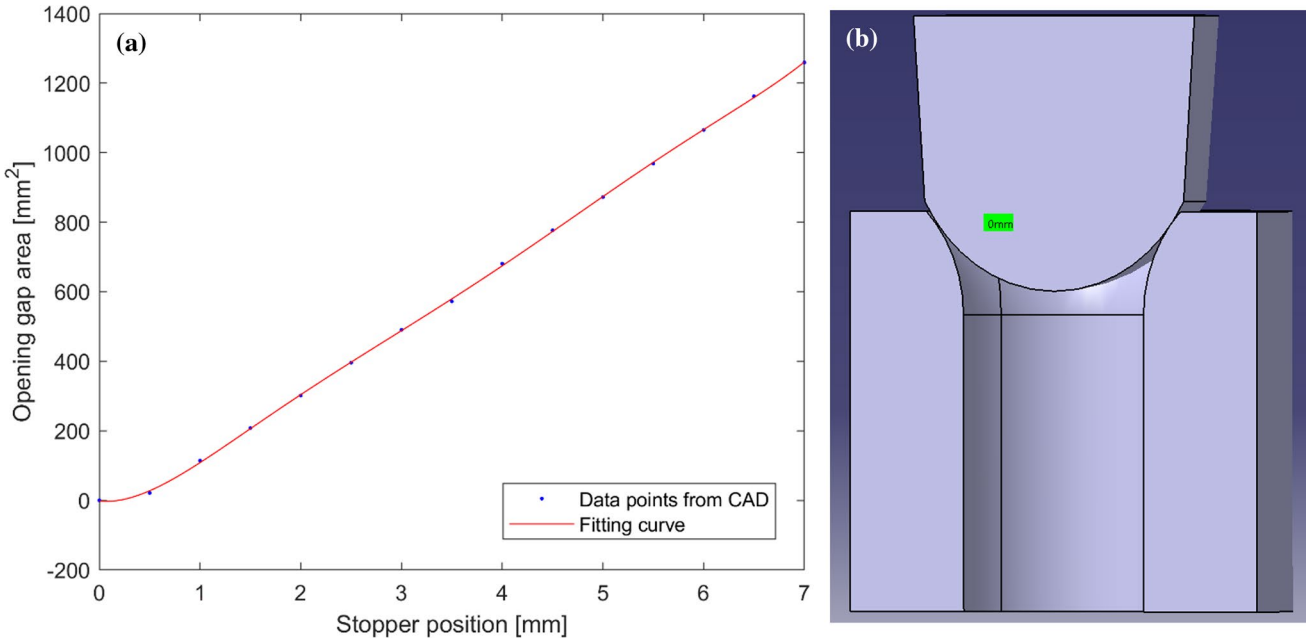

Fig. 5 **a** Polynomial function for the opening gap area of the SEN inlet A_{gap} versus stopper position and **b** CAD geometry used to measure the minimum distance and opening area of the gap

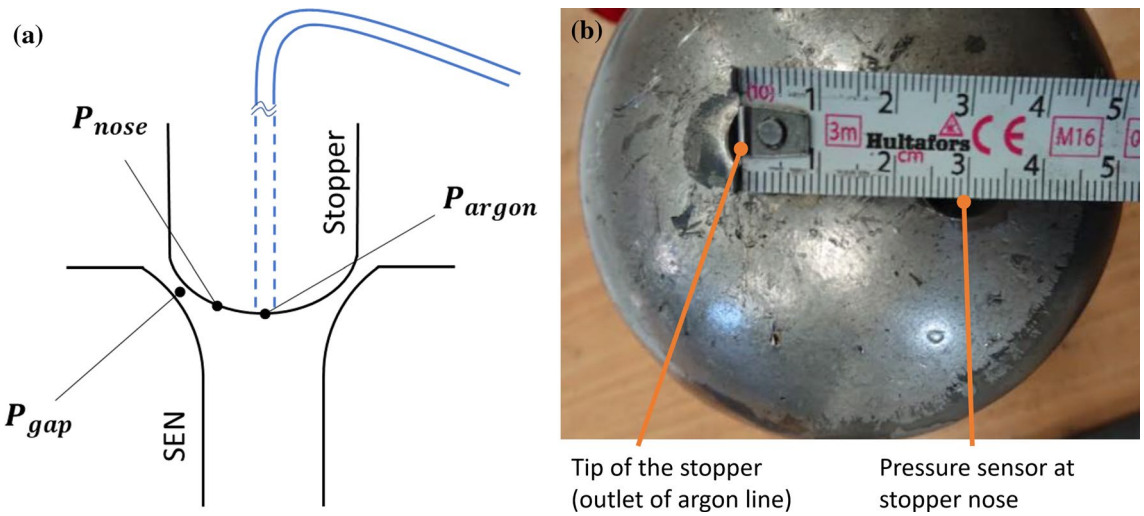

Fig. 6 **a** Schematic of the measured pressure points (P_{argon} and P_{nose}) and calculated pressure point (P_{gap}) and **b** actual location of the pressure points on the stopper nose

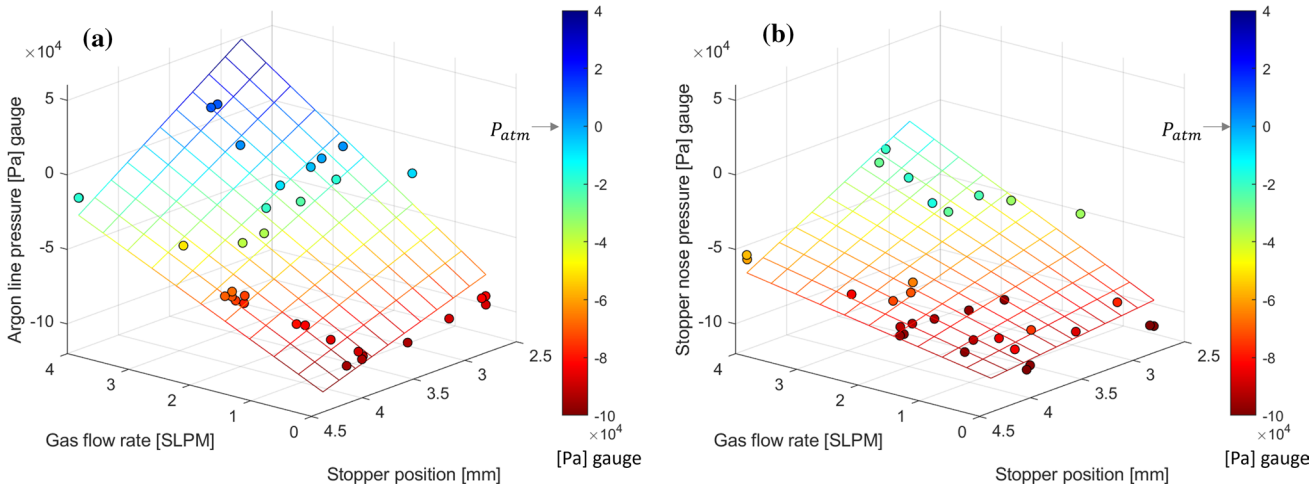

Fig. 7 Measured pressures at **a** argon line and **b** stopper nose at various stopper positions and gas flow rates

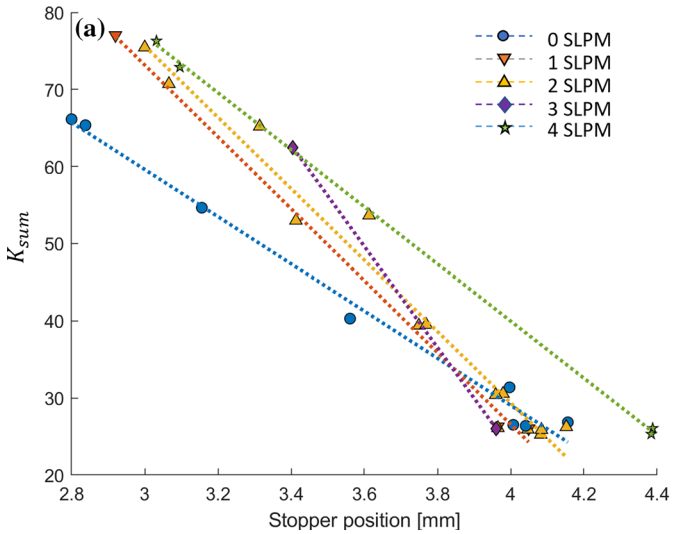

(b)

Q_{argon}	K_{sum}
0 SLPM	$-30.5712 \times h_{stopper} + 151.3248$
1 SLPM	$-46.5991 \times h_{stopper} + 212.9598$
2 SLPM	$-46.2886 \times h_{stopper} + 214.5131$
3 SLPM	$-65.5781 \times h_{stopper} + 285.7338$
4 SLPM	$-37.0077 \times h_{stopper} + 188.0006$

Fig. 8 **a** Characterized pressure loss K_{sum} and **b** regression equations obtained for various stopper positions and gas flow rates

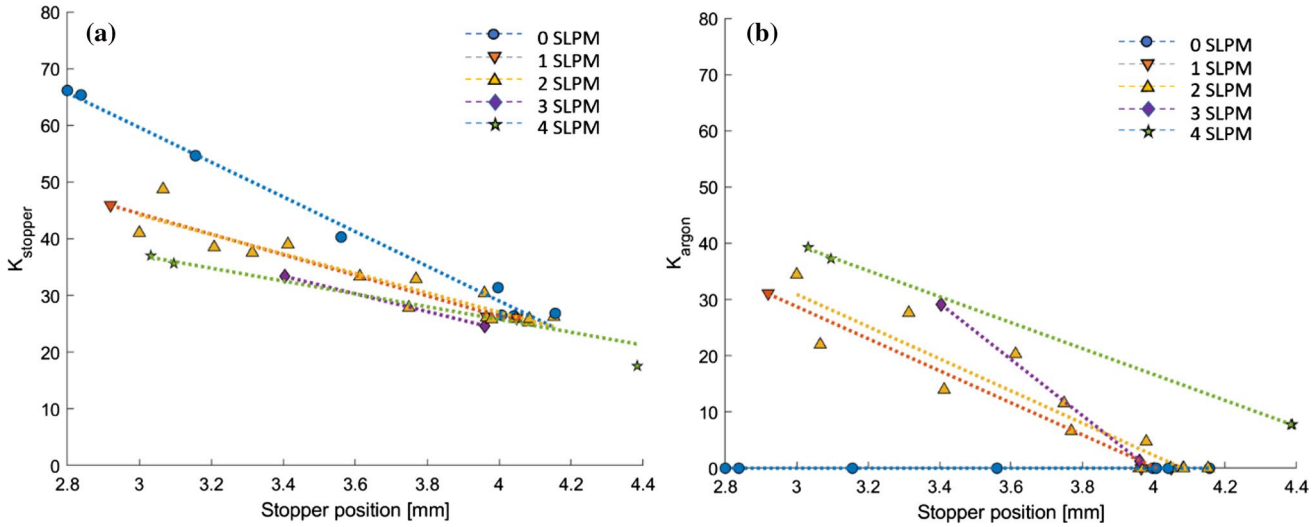

Fig. 9 Characterized pressure loss **a** $K_{stopper}$ and **b** K_{argon} for various stopper positions and gas flow rates

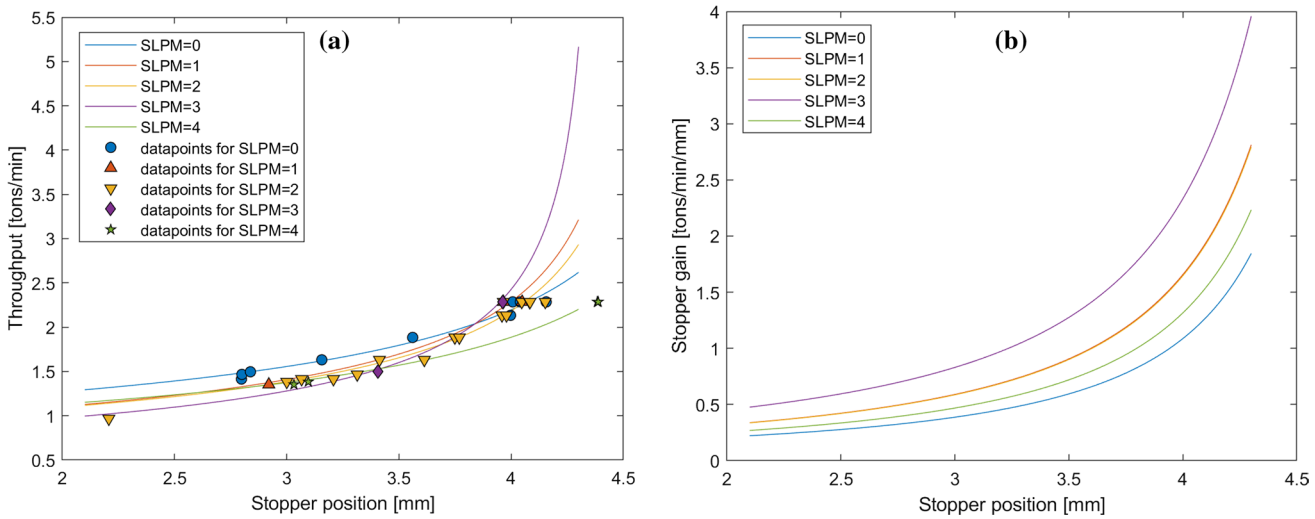

Fig. 10 **a** Estimated throughput and **b** stopper gain for various stopper positions and gas flow rates

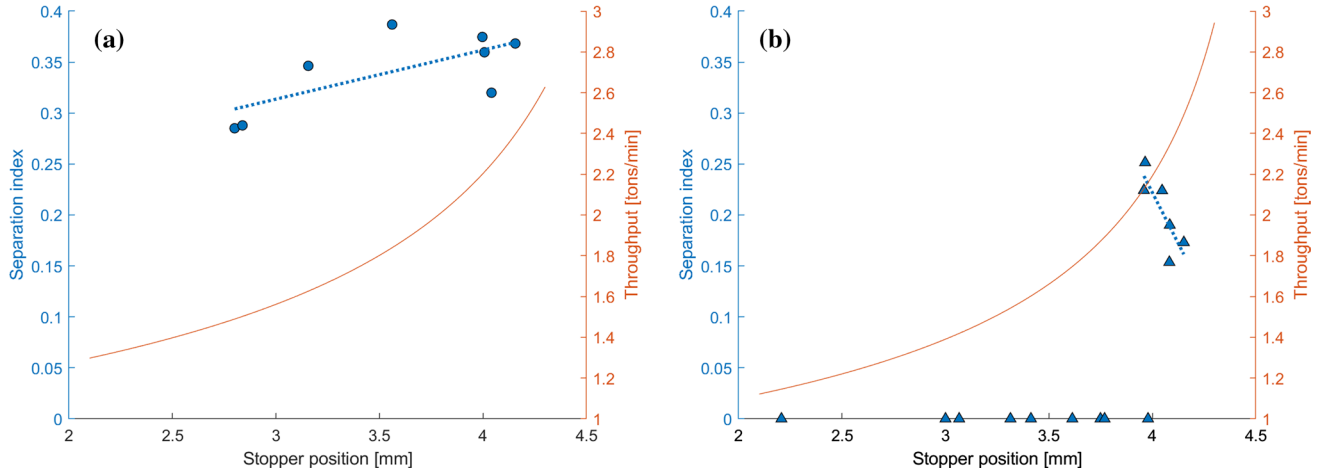

Fig. 11 Separation index and throughput for a stopper position for gas flow rates of **a** 0 SLPM and **b** 2 SLPM

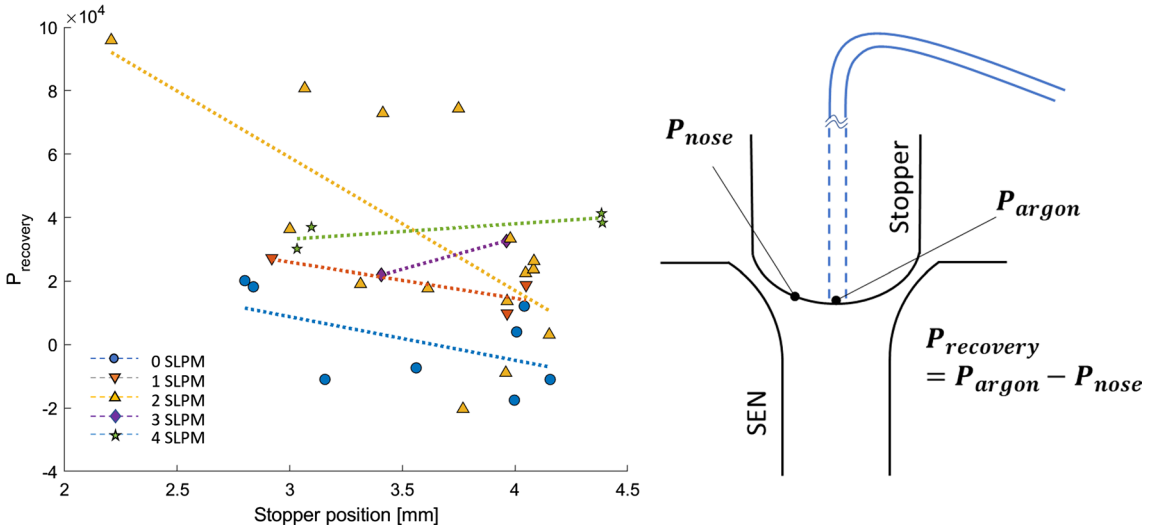

Fig. 12 Measured pressure recovery for various stopper positions and gas flow rates

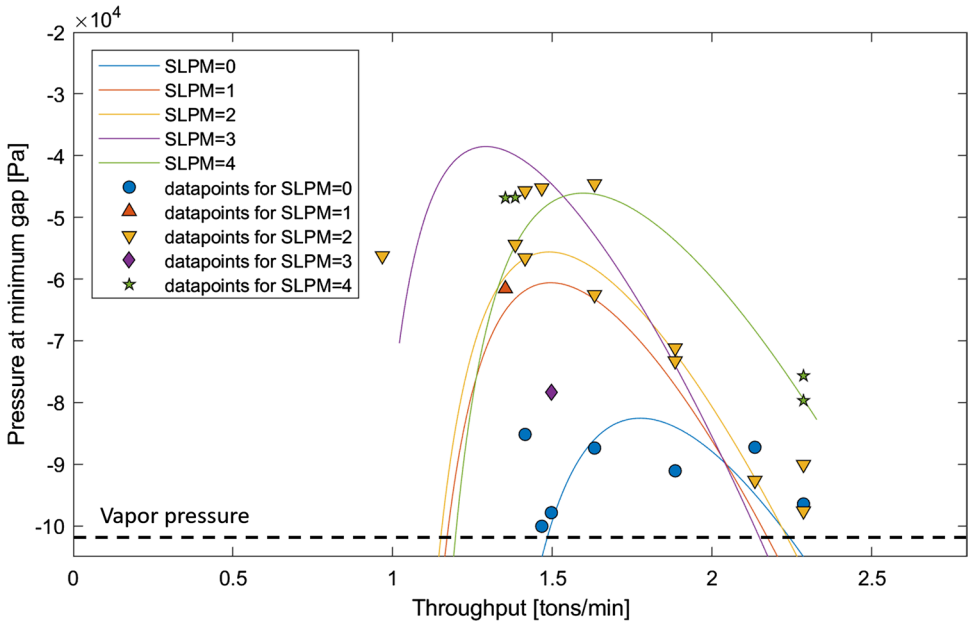

Fig. 13 Relationship between throughput Q_{metal} and minimum gap pressure P_{gap}

Table 3 Correlation analysis between process variables and pressure-related outputs

	P_argon	P_gap	P_recovery	K_sum	K_stopper	K_argon	Separation #
h_stopper	−0.434942212	−0.57677	−0.4068233	−0.930791945	−0.904845505	−0.70896	0.270885822
Gas fraction	0.870854829	0.653473	0.5518306	0.445719864	0.012363425	0.745254	−0.823154667

Acknowledgements This work was supported by an INHA UNIVERSITY Research Grant. This work was supported by Korea Institute of Energy Technology Evaluation and Planning(KETEP) grant funded by the Korea Government(MOTIE).(RS-2023-00243974, Graduate School of Digital-based Sustainable Energy Process Innovation Convergence).

Declarations

Conflict of interest The authors have no relevant financial or non-financial interests to disclose.

References

1. R.M.C. De Keyser, Control. Eng. Pract. **5**, 231–237 (1997)
2. H. Jeong, J.-Y. Hwang, J.-W. Cho, Met. Mater. Int. **22**, 295–304 (2016)
3. M. Jeong, C. Choi, M.Y. Ha, S.J. Kim, J.K. Park, K.S. Oh, Met. Mater. Int. **21**, 303–310 (2015)
4. H. Yang, S.P. Vanka, B.G. Thomas, ISIJ Int. **59**, 956–972 (2019)
5. S. Yokoya, S. Takagi, H. Souma, M. Iguchi, Y. Asako, S. Hara, ISIJ Int. **38**, 1346–1352 (1998)
6. H. Bai, B.G. Thomas, Metall. Mater. Trans. B **32**, 707–722 (2001)
7. J. Savolainen, A. Rousu, T. Fabritius, O. Mattila, P. Sulasalmi, Steel Res. Int. **81**, 980–986 (2010)
8. H. Yang, H. Olia, B.G. Thomas, Metals **11**, 116 (2021)
9. M. Suzuki, Y. Yamaoka, N. Kubo, M. Suzuki, ISIJ Int. **42**, 248–256 (2002)
10. H. Yang, S.P. Vanka, B.G. Thomas, JOM **70**, 2148–2156 (2018)
11. M. Javurek, M. Thumfart, R. Wincor, Steel Res. Int. **81**, 668–674 (2010)
12. B.F. Armaly, F. Durst, J.C.F. Pereira, B. Schönung, J. Fluid Mech. **127**, 473–496 (1983)
13. R.C. Lima, C.R. Andrade, E.L. Zaparoli, Int. Commun. Heat and Mass Transfer **35**, 1053–1060 (2008)
14. F. Durst, C. Tropea, *Structure of Complex Turbulent Shear Flow*, ed. by R. Dumas, L. Fulachier (Springer, Berlin, 1983), pp.41–52
15. T. Kato, M. Hara, A. Muto, S. Hiraki, M. Kawamoto, ISIJ Int. **47**, 840–846 (2007)
16. R.B. Fdhila, Analyse expérimentale et modélisation d'un écoulement vertical à bulles dans un élargissement brusque, Ph.D. Thesis, National Polytechnic Institute of Toulouse (1991)
17. F. Aloui, L. Doubliez, J. Legrand, M. Souhar, Exp. Therm. Fluid. Sci. **19**, 118–130 (1999)
18. H. Bai, B.G. Thomas, Metall. Mater. Trans. B **32**, 1143–1159 (2001)
19. K. Timmel, N. Shevchenko, M. Röder, M. Anderhuber, P. Gardin, S. Eckert, G. Gerbeth, Metall. Mater. Trans. B **46**, 700–710 (2015)
20. M. Ishii, T. Hibiki, *Thermo-Fluid Dynamics of Two-Phase Flow* (Springer, New York, 2010)
21. K. Timmel, S. Eckert, G. Gerbeth, F. Stefani, T. Wondrak, ISIJ Int. **50**, 1134–1141 (2010)
22. H. Yang, Modeling of multiphase turbulent flow in continuous casting of steel, Ph.D. Thesis, University of Illinois (2018)
23. H. Yang, S.P. Vanka, B.G. Thomas, J. Fluids Eng. **140**, 101202 (2018)
24. N. Kasai, M. Iguchi, Tetsu-To-Hagane **91**, 847–855 (2005)
25. M. Iguchi, J. Yoshida, T. Shimizu, Y. Mizuno, ISIJ Int. **40**, 685–691 (2000)

26. N. Bessho, R. Yoda, H. Yamasaki, T. Fujii, T. Nozaki, S. Takatori, ISIJ Int. **31**, 40–45 (1991)
27. K. Ishiguro, M. Iguchi, ISIJ Int. **43**, 663–670 (2003)
28. S.R. Higson, P. Drake, M. Lewus, T. Lamp, H. Kochner, P. Valentin, C. Brush, J. Ciriza, J.J. Lauraudogoitia, J. Bjorkvall, L. Bergman, *Flowvis: Measurement, Prediction and Control of Steel Flows in the Casting Nozzle and Mould* (European Commission, Brussels, 2010)
29. R. Liu, B.G. Thomas, J. SenGupta, S.D. Chung, M. Trinh, ISIJ Int. **54**, 2314–2323 (2014)
30. M. Iguchi, Y. Terauchi, Int. J. Multiphas. Flow **27**, 729–735 (2001)
31. B.G. Thomas, X. Huang, R.C. Sussman, Metall. Mater. Trans. B **25**, 527–547 (1994)